

PCCP

Accepted Manuscript



This is an *Accepted Manuscript*, which has been through the Royal Society of Chemistry peer review process and has been accepted for publication.

Accepted Manuscripts are published online shortly after acceptance, before technical editing, formatting and proof reading. Using this free service, authors can make their results available to the community, in citable form, before we publish the edited article. We will replace this *Accepted Manuscript* with the edited and formatted *Advance Article* as soon as it is available.

You can find more information about *Accepted Manuscripts* in the [Information for Authors](#).

Please note that technical editing may introduce minor changes to the text and/or graphics, which may alter content. The journal's standard [Terms & Conditions](#) and the [Ethical guidelines](#) still apply. In no event shall the Royal Society of Chemistry be held responsible for any errors or omissions in this *Accepted Manuscript* or any consequences arising from the use of any information it contains.



Journal Name

ARTICLE

Ni on the CeO₂ (110) and (100) Surfaces: Adsorption vs. Substitution Effects on the Electronic and Geometric Structures and Oxygen Vacancies

Received 00th January 20xx,
Accepted 00th January 20xx

DOI: 10.1039/x0xx00000x

www.rsc.org/

W.Q. Li,^{a,b} S. Goverapet Srinivasan,^a D. R. Salahub^a and T. Heine^{b,c}

We report Density Functional Theory (DFT) calculations of the interactions of both Ni adsorbate and substitutional dopant with the ceria (110) and (100) surfaces to explain the origin of the activity of Ni/Ceria catalysts. Our results indicate that the Ni adatom on the (110) surface prefers to adsorb on a two-fold bridge site over a hollow site up to 0.25 ML coverage, and the most stable position of a Ni adsorbate on the (100) surface was found to be the bridge site where the Ni atom is coordinated to two surface O atoms. The Ni⁺ oxidation state for the Ni adatom on the (110) surface was found to be more favorable than the Ni²⁺ state on the two-fold bridge site while on the (100) surface, a Ni adatom prefers its Ni²⁺ oxidation state over the Ni⁺ oxidation state. With increasing coverage, the binding energy of a Ni adatom on the (110) surface was found to decrease from -0.45 eV at 0.083 ML coverage to -0.32 eV at 0.25 ML coverage. Oxidation of the Ni adatom to Ni⁺ reduces one Ce⁴⁺ ion on the ceria surface to Ce³⁺ which preferred to be located next to the Ni⁺ ion in the nearest neighbor location. The Ce³⁺ ions on the (100) surface also prefer to stay in the vicinity of the adsorbed Ni atom, while they prefer to be located away from the Ni adatom on the (111) surface. No reduction of Ce⁴⁺ ions was observed upon substitution of Ce atoms by Ni atoms. Two Ni substituents preferred to be distributed on adjacent metal ion sites on the (110) surface. Ni adsorbate and substituent on the (110) surface were both found to induce significant structural distortions. In comparison to the pure ceria (110) and (100) surfaces, we show that a Ni adsorbate increases the energy required to create an oxygen vacancy while a Ni dopant reduces it. While multiple dopants on the (110) surface do reduce the vacancy formation energy, the degree of reduction is smaller compared to a single dopant indicating the presence of an optimum level of doping to obtain enhanced catalytic activity.

1. Introduction

Owing to its ability to cycle oxygen through redox processes and high oxygen ion mobility, ceria based compounds have been used in a variety of applications ranging from catalysts for the treatment of automobile exhausts and industrial pollutants¹⁻³ to the water gas shift (WGS) reaction³⁻⁵ and as solid electrolytes in solid oxide fuel cells⁶. The ability of ceria to cycle oxygen efficiently originates from the relative ease of the reversible removal of an oxygen ion from the surface. The formation of an oxygen vacancy results in the partial reduction of lattice cerium ions from the Ce⁴⁺ to the Ce³⁺ oxidation state.

Numerous studies, both theoretical and experimental, have been carried out in the past to characterize the role of ceria in such applications and develop novel catalysts with higher activity. Often ceria has been used in combination with other transition metals (e.g. Pd, Pt, Au etc.) or transition metal oxides (e.g. VO_x) to achieve enhanced catalytic performance. For instance, a higher activity was shown by ceria-supported VO_x catalysts for the oxidative dehydrogenation of methanol^{7, 8}, ceria-supported Au⁹ and Pt^{10, 11} catalysts for CO oxidation, ceria-supported Cu, Au, Pt, Pd, Rh^{4, 5, 12-15} for the WGS reaction etc. More recently, it has been shown that the Ni/CeO₂ system has an exceptional activity and selectivity for both WGS and ethanol steam reforming reactions¹⁶⁻²⁰. A detailed review of the theoretical approaches used to study ceria and heteroatom doped ceria surface energies, catalysis by ceria and their comparison to experiments was presented in a recent article by Sauer et al²¹

The geometric and electronic structure changes induced by a hetero metal atom on a metal oxide support have been described traditionally via 'strong metal support interaction'²²⁻²⁴. To explain the enhanced catalytic activity of transition metal/ceria catalysts, firstly it is necessary to gain a

^a Department of Chemistry, Centre for Molecular Simulation and Institute for Quantum Science and Technology, University of Calgary, AB T2N 1N4, Canada

^b Department of Physics and Earth Science, Jacobs University Bremen, Campus Ring 1, 28759 Bremen, Germany

^c Wilhelm-Ostwald-Institut für Physikalische und Theoretische Chemie, Universität Leipzig, Linnéstr. 2, 04103 Leipzig, Germany

† Electronic Supplementary Information (ESI) available: The optimal structures along with their formation energies for various Ni/CeO₂ (110), (100) and (111) systems are provided. See DOI: 10.1039/x0xx00000x

fundamental understanding of the interaction of the metal particle with the ceria support. Towards this end, a number of studies in the past have been carried out. Most of these studies have, however, focused on the adsorption of metal ions on the CeO₂ (111) surface, which is the most stable surface²⁵ amongst the low-index ceria surfaces (i.e., (100), (110) and (111) surfaces). Metal-atom adsorbates that were studied include Cu²⁶⁻²⁹, Ag^{26, 29}, Au^{26, 29, 30}, Pt³¹⁻³³, Pd^{33, 34}, Rh³³, and Ni^{19, 28}. All these metal atoms adsorbed strongly on the (111) surface and were found to be oxidized. The oxidation of the metal adsorbates resulted in the partial reduction of one or more lattice Ce⁴⁺ ions to Ce³⁺, with the unpaired electrons localizing on the Ce 4*f* orbitals. An Au adsorbate was found to have a number of competing states with Au⁺ and Au⁰ oxidation states of the metal lying close in energy³⁵. While the (111) surface is the most stable of the low index ceria surfaces, ceria nanorods often expose the more reactive and less stable (110) and (100) surfaces^{36, 37}. As such, an understanding of the interaction of metal adsorbates with (110) and (100) surfaces is essential to explain the origin of their activity. Very few studies in the past have investigated the interaction of transition-metal adsorbates with the (110) and (100) surfaces. Adsorption of Cu, Ag and Au on ceria (110) was reported by Cui et al³⁸ while Nolan³⁹ reported the adsorption of a series of 3rd row transition metals (V, Cr, Fe), *d*¹⁰ metals (Cu, Ag and Au) and trivalent cations (Al, Ga, In, La). It was found that all the transition metals were oxidized (Cu, Ag and Au to their 1+ oxidation states, V and Cr to their 3+ oxidation states, Fe to its 2+ oxidation state) with the partial reduction of an equivalent number of lattice Ce⁴⁺ ions to Ce³⁺. It was found that amongst the studied transition metals, Cu had the largest adsorption energy. Also, the *d*¹⁰ metals adsorbed more strongly on the (110) surface compared to other transition metals. Amongst the trivalent cations, Al and La were oxidized to their 3+ oxidation states while Ga and In were only partially oxidized to their 2+ oxidation states. On the other hand, to the best of our knowledge, a detailed investigation of the adsorption of Ni on ceria (110) and (100) is yet to be undertaken. Experimentally it is known that Ni particles anchor more strongly on the (110) and (100) surfaces as compared to the (111) surface⁴⁰. In addition, recent experiments²⁰ have shown that the oxidation state of Ni particles on ceria (111) could vary from Ni²⁺ to Ni⁰ depending on their surface coverage. Thus, any theoretical investigation of a transition-metal adsorbate on ceria surfaces must take into account the possibility of the presence of many competing close-lying oxidation states of the metal adsorbate. Finally, doping of ceria surfaces has also been considered as a way to enhance the oxidative capacity of the ceria surface⁴¹. Thus, a number of studies in the past have attempted to understand the modifications to the surface properties induced by transition-metal substituents. Doping of ceria surfaces with Mn⁴², Ti, Zr and Hf⁴³, La⁴⁴, Ni and Pd⁴⁵ resulted in a strong distortion of the surface induced by the substituents along with a reduction in the energy required for the creation of an oxygen vacancy.

In this article, we have carried out a detailed analysis of the interaction of a Ni adsorbate and a substituent with the

ceria (110) and (100) surfaces. Considering the points mentioned above, in this article we have attempted to answer the following questions:

1. What are the preferred adsorption site and oxidation state for a Ni adsorbate?
2. What is the adsorption energy of a Ni adsorbate and how does it compare with the adsorption energies of the other transition metal atoms reported in the literature?
3. What is the nature of the distortions induced in the geometric and electronic structure of the surface by the Ni adsorbate?
4. How do the above quantities vary as a function of the surface coverage of the Ni adsorbate?
5. How do multiple Ni substituents prefer to distribute themselves and how do they compare with a mono-Ni substituent?
6. How is the oxygen vacancy formation energy affected by Ni adsorption and substitution?

Section 2 describes the details of the computational methods used in this work while section 3 discusses our results. Conclusions from this work are presented in section 4.

2. Computational methods and details

DFT calculations have been performed to understand the interaction of Ni adsorbate/substituents with the ceria surface. All the calculations were performed using the VASP software⁴⁶⁻⁴⁹. The valence electronic states were expanded in a basis of plane waves. The core-valence interaction was described through the Projector Augmented Wave (PAW) approach^{50, 51}. A plane wave kinetic energy cutoff of 400 eV was used. The Perdew-Burke-Ernzerhof (PBE) GGA was used to describe the exchange-correlation interactions. The DFT+U⁵² approach was used to describe the localized 4*f* and 3*d* electronic states in Ce and Ni respectively. In line with earlier works^{53, 54}, we choose a Hubbard-U value of 4.5 eV and 4.6 eV for the Ce 4*f* and Ni 3*d* states respectively. The Hubbard-U value results in a lattice constant of 5.44 Å for bulk CeO₂ (fluorite structure, *Fm* $\bar{3}$ *m* space group), 3.83 Å and 6.01 Å (*a* and *c* lattice parameter values) for bulk Ce₂O₃ (*P* $\bar{3}$ *m*1 space group), 4.17 Å for bulk NiO (*Fm* $\bar{3}$ *m* space group) in close agreement with the experimental values of 5.41 Å for CeO₂, 3.89 Å and 6.06 Å for Ce₂O₃, and 4.17 Å for NiO. Our computed lattice parameters agree well with earlier reported values for CeO₂ (5.48 Å)⁵⁴, Ce₂O₃ (3.87 and 5.93 Å)⁵⁵ and NiO (4.19 Å)⁵⁶. All our calculations utilized 'accurate' precision settings in VASP. Complete cell optimizations and a re-relaxation for the bulk systems were performed to avoid any artifacts due to Pulay stress. Spin-orbit coupling (SOC) was not considered since our calculations indicated that the inclusion of SOC has only a minor effect on the electronic structure, for instance the band gap of CeO₂ changes only by 70 meV (see figure S1 in supporting information). We have also ignored the effect of variations in energy due to different occupations of the *m* projections of the 4*f* orbitals on Ce and 3*d* orbitals on Ni⁵⁷. Table T1 in the supporting information gives a comparison of the results obtained with DFT/PBE, DFT/PBE+U and

experiment. Clearly, our method of choice (DFT/PBE+U) is in much better agreement with experiments as compared to DFT/PBE.

In order to study the effect of Ni adsorbate coverage on Ni/ceria interactions, 3D boundary conditions were used throughout and, hence, the surfaces were modelled using the repeated slab method in which a finite number of crystal layers are used to generate two identical surfaces via the introduction of a vacuum gap perpendicular to the surface. In the case of the (110) surface, two different CeO₂ (110) surface models, a (2×1) surface and a (3×2) surface, were considered. Both the surfaces were generated from a conventional CeO₂ unit cell consisting of 12 atoms (4 Ce atoms and 8 O atoms in a fluorite structure with *Fm* $\bar{3}$ *m* space group). The (2×1) surface model consisted of 60 atoms (20 Ce atoms and 40 O atoms) with simulation box sizes of 10.89 Å × 7.7 Å, while the (3×2) surface model consisted of 180 atoms (60 Ce atoms and 120 O atoms) with box sizes of 16.33 Å × 15.4 Å. Both the slabs were 5 atomic layers thick and a vacuum gap of 15 Å was used in the direction perpendicular to the surface. Thus, the surface layer of the (2×1) slab contained 4 Ce atoms while that of the (3×2) slab contained 12 Ce atoms. Adsorption of one Ni atom then corresponds to a coverage of 0.25 ML on the (2×1) surface and 0.083 ML on the (3×2) surface. Interactions of a Ni substituent with the CeO₂ (110) surface were studied for the larger (3×2) surface only. Mono-substitution and di-substitution of surface Ce atoms with Ni atoms were considered to investigate the effect of the Ni substituent concentration. Thus, mono-substitution corresponds to 8.3% Ni concentration, while di-substitution corresponds to 16.6% Ni concentration at the surface. The (100) surface was modelled as an oxygen-terminated surface with half of the oxygen atoms in a chessboard-like arrangement. It is stoichiometric and has been found to be the most stable polar-compensated (100) plane in the past⁵⁸. A (3×3) expansion of the (100) surface was used for our calculations, and includes 11 atomic layers and 135 atoms (45 CeO₂ units) with simulation box sizes of 11.54 Å × 11.54 Å. Adsorption of one Ni atom then corresponds to a coverage of 0.111 ML. Mono-substitution corresponds to 11.1% Ni concentration at the surface. These models were further used to compute the formation energies of charge-compensating and active O vacancies.

For the (100) surface, the atomic coordinates of all the atoms were allowed to relax fully, but for the (110) surface, atoms in the bottom two layers were frozen at their bulk positions due to the large size of the system (180 atoms). For both the slabs, the lattice parameters were fixed at the above-mentioned values during optimization. Geometry optimizations were deemed to have converged when the forces dropped below 0.03 eV Å⁻¹. For the electronic structure, the SCF energy convergence was set to a threshold of 10⁻⁵ eV. A Pulay mixing scheme⁵⁹ as implemented in VASP was used for charge-density mixing in the SCF solution. For the (3×3) slab of the (100) surface, during geometry optimization, the Brillouin zone was sampled using a 2×2×1 Monkhorst-Pack (MP) grid. For the (2×1) slab of the (110) surface, the Brillouin zone was sampled using a (1×2×1) MP *k*-point mesh. Later, a finer

(4×6×1) MP *k*-point mesh was used to compute the energies at the optimized structure. For the (3×2) slab of the (110) surface, the Brillouin zone was sampled using the Γ -point approximation.

CeO_{2(s)}, Ni_(s), Ce_(s) and O_{2(g)} were used as the reference to compute the formation energies in equations (1) – (8). Calculations on the face-centered cubic (fcc) Ni_(s) and γ -Ce_(s) were performed on a one-atom unit cell using a 16 × 16 × 16 Monkhorst-pack *k*-point mesh, resulting in an optimized lattice parameter of 3.474 Å for Ni_(s) and 5.208 Å for Ce_(s), in good agreement with the experimental value of 3.52 Å and 5.16 Å respectively. The local magnetic moment on the Ni atom in Ni_(s) was found to be ~0.78 μ_B while it was ~1 μ_B on the Ce atom in Ce_(s). Calculations on the O_{2(g)} molecule were performed in a 10 Å × 10 Å × 10 Å box in the triplet state using the Γ -point approximation to sample the Brillouin zone. The optimized O₂ bond length was found to be 1.234 Å.

3. Results and discussion

In bulk CeO₂ (fluorite structure, *Fm* $\bar{3}$ *m* space group), Ce⁴⁺ and O²⁻ are characterized by eight- and four-fold coordination, respectively. The relaxed O-Ce bond length of 2.355 Å is close to the experimental value of 2.343 Å. The CeO₂ (110) surface consists of six-coordinated Ce⁴⁺ ions and three-coordinated O²⁻ ions. On the (100) surface, Ce⁴⁺ and O²⁻ are six- and two-coordinated, respectively. The relaxed surface was found to have a Ce-O bond length of 2.326 Å on the (110) surface and 2.191 Å on the (100) surface. We have also investigated the CeO₂ (111) surface, in which Ce⁴⁺ and O²⁻ are seven- and three-coordinated, respectively. The O-Ce bond length 2.360 Å is close to the bulk O-Ce bond length 2.355 Å. The surfaces were diamagnetic with all the Ce ions in their Ce⁴⁺ oxidation state and O ions in their O²⁻ oxidation state. The surface energies of CeO₂ (110), (100) and (111) were found to be 1.06, 1.44 and 0.60 J/m², respectively. They are in very good agreement with earlier reported values (1.06 J/m² for (110), 1.44 J/m² for (100) and 0.68 J/m² for the (111) surface) in the literature^{25, 60-62}. It is known that the order of stability of CeO₂ low index surfaces is CeO₂ (111) > CeO₂ (110) > CeO₂ (100)²⁵.

3.1 Ni adsorption on CeO₂ surfaces

A. Ni adsorption on CeO₂ (110): preferred adsorption site

A few previous articles^{38, 39, 63} have reported the adsorption of transition metal atoms on the CeO₂ (110) surface. It was shown that the preferred adsorption site was a bridge site, connecting two surface O atoms. We have studied the adsorption of a Ni atom on a bridge site and a hollow site (where the adsorbate is coordinated to four surface O atoms), as shown in Figure 1. The (2×1) CeO₂ (110) slab was used for these calculations, corresponding to a Ni coverage of 0.25 ML. Recent experiments²⁰ on the Ni/CeO₂ (111) surface indicated that the oxidation state of the adsorbed Ni atom could vary from Ni²⁺ to Ni⁰ depending on the coverage of Ni. At lower coverages, the Ni atom was found to be oxidized to Ni²⁺. As the

coverage approached unity, the Ni atom seemed to remain in the Ni⁰ oxidation state.

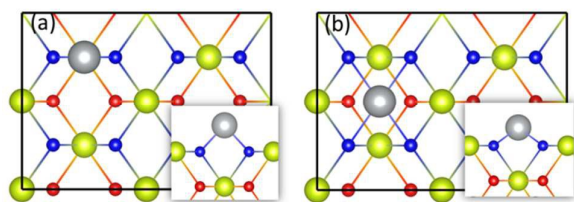


Figure 1: Initial structures of Ni adsorption on the ceria (110) surface. (a) Bridge site (b) Hollow site. Insets show the front view of the structures. Ce atoms are yellow, O atoms are red and blue, Ni atom is grey. In order to distinguish the surface O atoms from other O atoms in the slab, they are shown in blue colour.

Thus, in addition to the adsorption site, any detailed analysis of the interaction of a transition-metal adsorbate on CeO₂ surfaces must consider the oxidation state of the adsorbed transition metal atom. As such, we have studied configurations where the Ni atom is in its Ni⁺ and Ni²⁺ oxidation states on both the bridge and hollow sites. In its Ni⁺ oxidation state, the Ni atom donates an electron from its 4s orbital to the 4f orbital of a surface Ce, thereby reducing it from Ce⁴⁺ to Ce³⁺. Similarly, when Ni is in its Ni²⁺ oxidation state, two surface Ce are reduced from Ce⁴⁺ to Ce³⁺. It is now well known that the reduced Ce³⁺ could be located in one or more of the many surface metal ion sites and various configurations must be investigated to determine the most favorable distribution of Ce³⁺ on the surface. In order to do so, we have followed the procedure outlined by Kullgren et al.⁶⁴ First we perform a geometry optimization using a different PAW potential (where the Ce 4f electron is included in the core) on those Ce atoms that we wish to be reduced to Ce³⁺, while the rest of the Ce atoms use the full valence pseudopotential. In the second step we continue the optimization from the converged structure in the previous step with all the Ce atoms described using the full valence

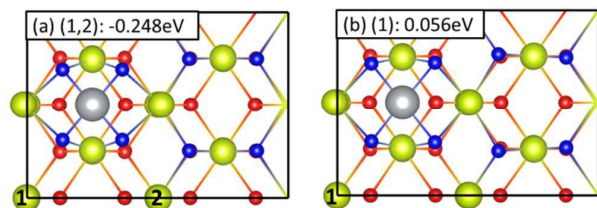
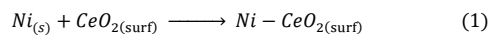


Figure 2: Adsorption of Ni on a hollow site on the CeO₂ (110) surface. (a) Ni is in its Ni²⁺ oxidation state with the two Ce³⁺ ions located at sites 1 and 2. (b) Ni is in its Ni⁺ oxidation state with the reduced Ce³⁺ ion located at site 1. Ce atoms are yellow, O atoms are red and blue, and Ni atom is grey.

pseudopotential. At the end of each calculation, the magnetizations on the Ce ions were checked to ensure that the reduced Ce³⁺ ion was located at the same position as chosen initially. This was done by looking at the local magnetization on the Ce³⁺ ion which should be ca. 1 μ_B due to an electron localized in its f orbital while the remaining Ce⁴⁺ ions have a magnetic moment of 0 μ_B. The reaction energy for the adsorption of a Ni atom on CeO₂ (110) was computed using equation (1):



Figures 2 and 3 show the optimized structures and reaction energies for the adsorption of Ni on hollow and bridge sites respectively. From figure 2 we see that on a hollow site, the Ni ion prefers a Ni²⁺ oxidation state over a Ni⁺ oxidation state, with the two reduced Ce³⁺ ions located at sites (1,2). The reaction energy for the adsorption of a Ni²⁺ ion on a hollow site at 0.25 ML coverage was found to be -0.248 eV while Ni⁺ adsorption was disfavored. The local structure around the Ni²⁺

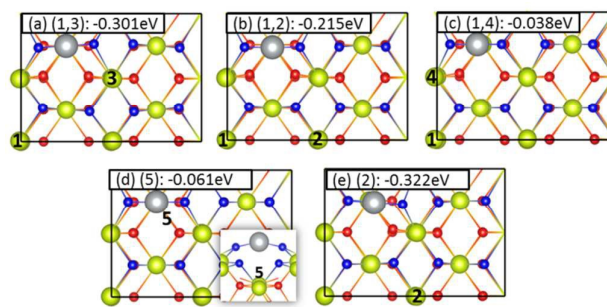


Figure 3: Adsorption of Ni on a bridge site on the CeO₂ (110) surface. (a-c) Ni is in its Ni²⁺ oxidation state with the two Ce³⁺ ions located at sites (1,3), (1,2) and (1,4) respectively. (d-e) Ni is in its Ni⁺ oxidation state with the reduced Ce³⁺ ion located at site 5 and 2 respectively. Inset in (d) shows the front view of the structure. Here, site 5 is the Ce ion beneath the Ni adatom. Ce atoms are yellow, O atoms are red and blue, Ni atom is grey.

ion was nearly planar with the four Ni-O bond lengths equal to 1.936 Å. Comparing this with the Ni-O bond length of 2.085 Å in solid NiO, we see that the Ni-O bond lengths are shortened upon adsorption of a Ni²⁺ ion on a hollow site. The four O²⁻ ions that coordinate with the adsorbed Ni²⁺ are pulled away from their normal positions on the surface, with the Ce³⁺-O²⁻ distance increased to 2.835 Å from 2.326 Å. On a bridge site, however (see Figure 3), we see that both Ni⁺ and Ni²⁺ oxidation states have stable configurations, with Ni⁺ being the preferred oxidation state. As mentioned earlier, for a given oxidation state of the adsorbate, various distributions of the reduced Ce³⁺ ions are possible. Here we have investigated three different Ce³⁺ distributions for Ni²⁺ adsorbate and two different distributions for Ni⁺ adsorbate, as shown in Figure 3. For the Ni²⁺ adsorbate, two Ce³⁺ ions located diagonally across the Ni²⁺ ion (at the (1,3) site as shown in Figure 3(a) on the surface was found to be the most favorable distribution, with a reaction energy of -0.301 eV. Upon adsorption, the two O atoms bridged by the Ni²⁺ ion are pulled outward from their location on the surface. This results in an elongation of the two O²⁻ - Ce⁴⁺ bonds to 2.464 Å from 2.326 Å. The two O²⁻-Ce³⁺ distances were 2.584 Å while the Ni²⁺ - O²⁻ bond distance was 1.69 Å. In comparison to Ni²⁺ adsorption on the hollow site, we notice that the distortions in the Ce - O bond lengths are smaller, resulting in a larger binding energy of the Ni²⁺ adsorbate on the bridge site. The least favorable distribution of Ce³⁺ ions for Ni²⁺ adsorbate was found to be at nearest neighbor locations (site (1,4) as shown in Figure 3c), which was ca. 263 meV less stable compared to Ce³⁺ located at the (1,3) site. For the Ni⁺ adsorbate on a bridge site, we have

investigated two different locations of the Ce^{3+} ion, a nearest-neighbor surface site (site 2, Figure 3e) and a subsurface site (site 5, Figure 3d). We find that the subsurface site is unfavorable while the nearest neighbor location for the Ce^{3+} ion results in adsorption energy of -0.322 eV. Adsorption of Ni^+ on a bridge site causes the O^{2-} coordinated to the Ce^{3+} ion to be pulled away from the surface significantly (by 1.23 Å with respect to CeO_2 (110)), resulting in a locally asymmetric structure around the Ni^+ adsorbate. Figure S2 in the supporting information shows the bond lengths surrounding the Ni^+ adsorbate. Thus, we find that a Ni adsorbate prefers the bridge site over the hollow site. Further, on the bridge site, the Ni adsorbate prefers the Ni^+ oxidation state, with the reduced Ce^{3+} located on the nearest neighbour surface site, over the Ni^{2+} oxidation state. The stabilization energy of the Ni^+ oxidation state over the Ni^{2+} oxidation state is ca. 21 meV. In addition, the Ni^+ adsorbate on the bridge site is ca. 74 meV more stable than the Ni^{2+} adsorbate on a hollow site. Thus, the preferred adsorption pattern for a Ni adsorbate on the CeO_2 (110) surface is:

$$\text{Ni}_{\text{bridge}}^+ > \text{Ni}_{\text{bridge}}^{2+} > \text{Ni}_{\text{hollow}}^{2+}$$

B. Ni adsorption on CeO_2 (110): Effect of surface coverage

Results from the previous section indicate that a Ni adsorbate prefers to adsorb on a bridge site in the Ni^+ oxidation state on the CeO_2 (110) surface. As mentioned earlier, experiments on Ni clusters adsorbed on the CeO_2 (111) surface²⁰ have indicated that the preferred oxidation state of Ni on CeO_2 (111) varies with the coverage of Ni. In order to study the effect of coverage on the oxidation state of the adsorbed Ni atom, we have investigated the adsorption of a Ni atom on a larger (3×2) CeO_2 (110) surface. We have studied adsorption on the bridge site only since results from the previous section indicated that the bridge site is preferred. Again, we have investigated a number of distributions of the Ce^{3+} ions on the surface, corresponding to a given oxidation state of the Ni adsorbate (i.e., 1 Ce^{3+} ion for the Ni^+ oxidation state and two Ce^{3+} ions for the Ni^{2+} oxidation state). Figure 4 shows the optimized structures along with the adsorption energies of the Ni adsorbate computed using equation (1).

From Figure 4, it is clear that on a larger (3×2) surface (corresponding to 0.083ML Ni coverage) as well, a Ni adsorbate prefers the Ni^+ oxidation state over the Ni^{2+} oxidation state. This is in contrast to Ni adsorption on the CeO_2 (111)¹⁹ and CeO_2 (100) surfaces, where the Ni adsorbate oxidizes to its Ni^{2+} state. The most favourable location of the reduced Ce^{3+} ion was found to be next to the adsorbed Ni^+ (see figure 4a) while locations far away from the adsorbed Ni^+ (see figure 4d) or the subsurface location were found to be unfavourable. For the Ni adsorbate in the Ni^{2+} oxidation state, similar to the structure found for the (2×1) slab above, two Ce^{3+} ions located diagonally across the Ni^{2+} adsorbate was found to be the most stable configuration. However, amongst the configurations studied here, while the energy difference between the least stable and the most stable Ce^{3+} distributions for Ni^+ adsorbate was ca. 795 meV, we find this value to be

reduced to only 97 meV for the Ni^{2+} adsorbate. Furthermore, comparing the above results with those on the smaller (2×1) slab (corresponding to 0.25ML Ni coverage) presented in the previous section, the following trends emerge:

1. As the coverage of Ni on the CeO_2 (110) surface increases from 0.083ML to 0.25ML , the adsorption energy for the most favourable configuration, i.e., Ni^+ on a bridge site, reduces from -0.449 eV to -0.322 eV.
2. With increase in coverage of Ni from 0.083ML to 0.25ML , the stabilization of the Ni^+ oxidation state over the Ni^{2+} oxidation state on a bridge site decreases from ca. 49 meV to 21 meV for the most preferred Ce^{3+} ion distribution in the respective oxidation states of the Ni adsorbate.
3. Amongst the configurations investigated here, with increase in coverage from 0.083ML to 0.25ML , the energy difference between the least and most stable Ce^{3+} distribution for the Ni^+ adsorbate decreases from ca. 795 meV to 383 meV, while this value increases from ca. 97 meV to 263 meV for the Ni^{2+} adsorbate.

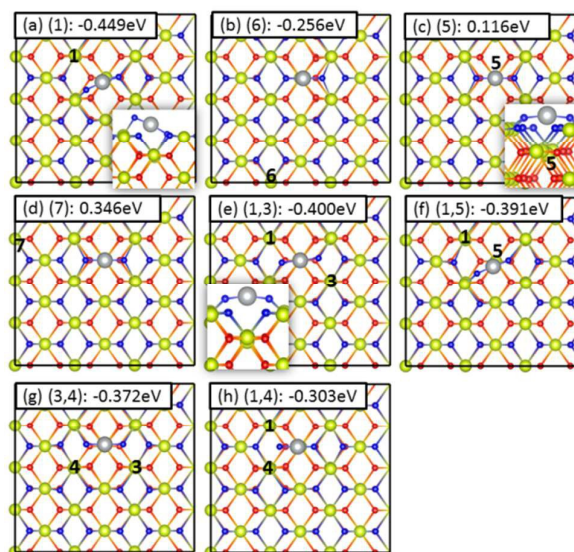


Figure 4: Adsorption of Ni on a bridge site on the CeO_2 (110) (3×2) surface. (a-d) Ni is in its Ni^+ oxidation state with the Ce^{3+} ion located at sites 1, 6, 5 and 7 respectively. (e-h) Ni is in its Ni^{2+} oxidation state with the two reduced Ce^{3+} ions located at sites (1,3), (1,5), (3,4) and (1,4) respectively. The insets in panels (a) and (e) show the front view of the structure. Ce ion is yellow, O atoms are red and blue, Ni atom is gray.

In comparison to the adsorption energies of other transition-metal atoms on the CeO_2 (110) surface³⁹, namely Au (-2.19 eV), Ag (-1.45 eV), Cu (-3.25 eV), V (-0.97 eV), Cr (-0.64 eV) and Fe (-0.75 eV), we find that Ni has the lowest adsorption energy amongst the transition metals reported so far. On the other hand, comparing the adsorption energy of a Ni atom on the CeO_2 (100) (-1.490 eV) and CeO_2 (111) (-0.185 eV) surfaces (see Table T2 in supporting information), we find that the order of stability of a Ni adsorbate on ceria surfaces is CeO_2 (100) > CeO_2 (110) > CeO_2 (111). This is in agreement with the experimental finding that the CeO_2 (110) and CeO_2 (100) surfaces bind Ni stronger than the CeO_2 (111) surface⁴⁰.

Figure 5 shows the total and projected density of states for a Ni adsorbate on a bridge site at 0.083ML coverage in

both Ni⁺ (figures 5a and 5b) and Ni²⁺ (figures 5c and 5d) oxidation states. The Fermi energy is set to 0 eV in all panels of Figure 5. The common feature in both cases is the appearance of split-off states above the valence band of CeO₂ (110) and right below the Fermi level. While for the Ni²⁺ adsorbate, this state arises almost exclusively from the two electrons localized on the 4*f* orbitals of the two reduced Ce³⁺ ions, for the Ni⁺ adsorbate this state arises from the combination of the 3*d* orbital of Ni⁺, 4*f* orbital on the reduced Ce³⁺ ion and the 2*p* orbitals on the two O²⁻ ions coordinating the Ni⁺ adsorbate.

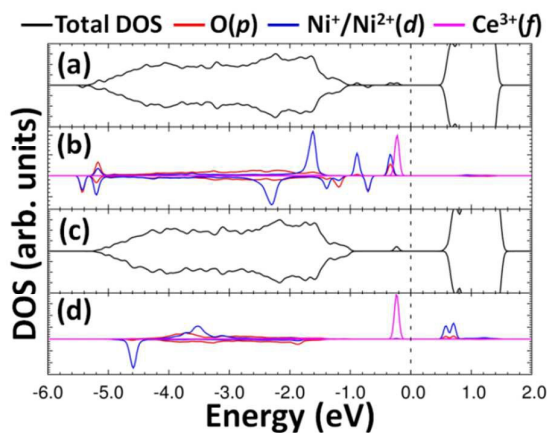


Figure 5: Total and projected density of States for the adsorption of Ni on CeO₂(110) bridge site at 0.083ML coverage. (a-b) Total and projected density of states for Ni adsorbate in Ni⁺ oxidation state. (c-d) Total and projected density of states for Ni adsorbate in Ni²⁺ oxidation state. The Fermi level is set to 0 in all the plots.

C. Ni adsorption on CeO₂ (100): preferred adsorption site

Two adsorption sites (a 2-fold site on top of a surface Ce atom and a bridge site on top of two surface O atoms) have been

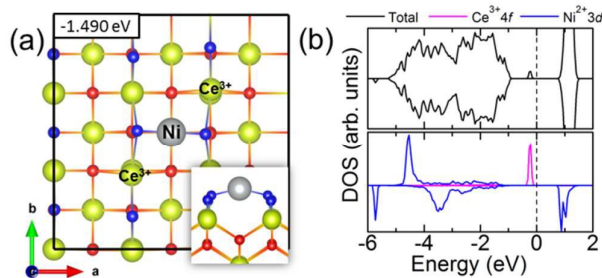


Figure 6: (a) The optimized atomic structure of Ni adsorbed on the CeO₂ (100) surface with the two Ce³⁺ ions located in the nearest neighbour locations. Inset shows the side view of the outermost four atomic layers. Ce atoms are yellow, O atoms are red and blue, Ni atoms is grey. (b) The total density of states (DOS) in the upper panel and projected DOS of Ce³⁺ 4*f* and Ni²⁺ 3*d* orbitals in the lower panel. The curves above (below) the horizontal axis correspond to spin-up (down) states. The Fermi level (the vertical dashed line) is set to zero.

explored for a single Ni adsorbed on the CeO₂ (100) surface. The most stable position was found to be the bridge site where the Ni atom is coordinated to two surface O atoms (see figure 6). In contrast to the (110) surface, Ni²⁺ state was found to be more stable than the Ni⁺ state on the (100) surface, resulting in the partial reduction of two surface Ce ions from Ce⁴⁺ to Ce³⁺. Imposing this constraint, we have systematically explored a range of possible

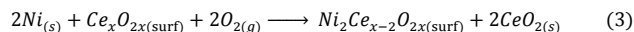
configurations for the Ce³⁺ pair (see figure S9 in supporting information). The most stable distribution of two Ce³⁺ ions on the (100) surface is shown in Figure 6. For this structure, the oxygen atoms surrounding Ni²⁺ relax outward, resulting in a O-Ce³⁺ bond length of 2.592 Å. The calculated O-Ce³⁺ bond lengths range from 2.324 to 2.666 Å, which is longer than the O-Ce⁴⁺ bond length of 2.191 Å on the pure (100) surface. The nearest-neighbour Ce⁴⁺ atoms around Ni²⁺ have O-Ce⁴⁺ bond lengths varying from 2.080 to 2.425 Å, leading to a large distortion of the surface. The two O-Ni bond lengths are 1.727 Å, which is much shorter than the O-Ni bond length (2.085 Å) in NiO. Therefore, a strong metal-support interaction is preferred. Figure 6 (b) shows the total and projected density of states for this structure. The main features are similar to the DOS of Ni²⁺ on the (110) surface. The two Ni 4*s* electrons are transferred to the empty Ce 4*f* orbitals that appear as split-off states from the Ce 4*f* band right below the Fermi level. The calculated local magnetic moment of Ce³⁺ is 0.97 μ_B, which is equal to the value 0.96 μ_B of Ce³⁺ in Ce₂O₃.

The Ce³⁺ ion prefers to be distributed around the Ni²⁺ adsorbate on the ceria (110) and (100) surfaces. This trend is in contrast to Ni²⁺ adsorbed on the ceria (111) surface¹⁹, where the Ce³⁺ ions strongly prefer to maximize their separation from the adsorbed Ni²⁺ ion (see Figures S14 and S15 in supporting information).

3.2 Ni substituent on CeO₂ surfaces

A. Ni substituent on CeO₂ (110): Mono- vs disubstitution and the formation of charge compensating oxygen vacancies

The previous section investigated the effects of the adsorption of a Ni atom on the CeO₂ (110) and (100) surfaces. In this section, results for a Ni-substituted CeO₂ (110) surface are discussed. We have considered the substitution of one surface Ce atom by a Ni atom and also the substitution of two surface Ce atoms by two Ni atoms in order to analyze how multiple substituents prefer to distribute themselves on the surface. The formation energy of mono and di Ni substituted surfaces were calculated using equations (2) and (3) respectively.



A number of different configurations for Ni substituents on the surface were examined to determine the most favourable location. Figure 7 shows the most favourable configuration of a mono- and di-Ni substituted surface while figure S3 in the supporting information shows the geometries of various other metastable structures along with their energies relative to the most favourable configuration shown in Figure 7.

Doping the surface with a Ni atom results in a strong distortion of the surface with the Ni substituent moving from the surface metal ion site into the ceria lattice by about 0.69 Å, consistent with the observations of Nolan⁴⁵. The local geometry around the Ni substituent was found to be nearly

planar with the Ni substituent coordinating with two surface- (designated by 'A' in figure 7a) and two subsurface O ions (designated by 'B' in figure 7a). The Ni-O_A distance was found to be 1.806 Å while the Ni-O_B distance was found to be 1.870 Å. For di-Ni substitution, the preferred distribution of the two Ni substituents was found to be at the nearest neighbour

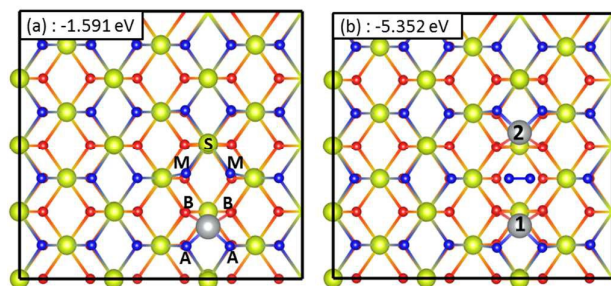
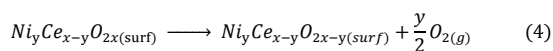


Figure 7: Ni substituent on CeO₂ (110) surface. (a) Optimum configuration for a mono substituent with four-coordinated Ni. (b) Optimum configuration for di Ni substituted surface. Ce atoms are yellow, O atoms are red and blue, Ni substituent is gray. 'S', 'M', 'A' and 'B' in (a) correspond to a surface Ce⁴⁺ ion, magnetic oxygen atoms, surface and sub-surface oxygen atoms respectively. 1, 2 in (b) correspond to the two Ni dopants.

positions as shown in figure 7b. This configuration resulted in the spontaneous formation of an O₂ molecule (see figure 7b) that remained adsorbed at around 1.9 Å above the surface. The O₂ molecule was found to be in a triplet spin state with a bond length of 1.238 Å, very close to the VASP-optimized bond length of 1.234 Å. Further we note that once a dopant is introduced, the energy cost associated with the introduction of a second dopant is reduced, compared to the first dopant (-1.591 eV vs -5.352 eV). In CeO₂, Ce ions are in an oxidation state of Ce⁴⁺ while O ions are in an oxidation state of O²⁻. Substituting a Ce⁴⁺ ion in CeO₂ (110) with a divalent cation results in a charge imbalance which is compensated by spin polarization of the oxygen ion (in the case of Ni substituent, mainly on those O ions marked with the label M in figure 7a), leading to partially unoccupied 'p' orbitals on these ions. The magnetic moment on the two O_M ions was found to be 0.37 μ_B while the magnetic moment on the Ni substituent was 0.92 μ_B, indicating that the Ni substituent does not get fully oxidized to the Ni²⁺ state. The total and projected density of states for the mono-Ni substituted surface is shown in figure S4 of the supporting information.

Another means to achieve charge neutrality is through the loss of one or more surface O atoms to form 'charge compensating' oxygen vacancies (one and two vacancies for mono- and di-Ni substituted CeO₂ (110) respectively). We have studied various distributions of charge compensating O vacancies on both the surfaces and computed their formation energy according to equation (4)



In the equation (4), $y = 1$ for the mono-Ni substituted surface and $y = 2$ for the di-Ni substituted surface. The most favourable location for the formation of a compensating O vacancy in mono-Ni substituted CeO₂ (110) was reported⁴⁵ to be from one of the O_M sites in figure 7a. We computed the O

vacancy formation energy using equation (4) to be -0.681 eV from the O_M site while Nolan⁴⁵ reported a value of only -0.24 eV. For the di-Ni substituted surface, a number of different locations for the compensating O vacancies were studied for different distributions of Ni dopants on the surface. For the most favourable (1, 2) distribution of the Ni dopants (see figure 7b), the compensating O vacancy formation energy was found to be -0.533 eV. However, it must be noted that this energy really corresponds to the molecular adsorption energy of O₂ on the surface rather than O-vacancy formation energy as the (1, 2) substitution of dopants led to a spontaneous ejection of an O₂ molecule as shown in figure 7b. In all the cases we notice that the Ni substituents continue to remain in a four coordinated environment even upon the formation of charge compensating vacancies.

B. Ni substituent on CeO₂ (100): Monosubstitution and the formation of charge compensating oxygen vacancies

We have also considered the structure of Ni substituted at a Ce site on the (100) surface, as shown in Figure 8. On the (100) surface, the Ni substituent is surrounded by six anions as the surface O is shared by two metal ions while an O in the bulk is shared by four metal ions. It is to be noted that Ni in NiO is coordinated to six O atoms, too. Upon relaxation, while Ni retains its six-fold coordination, the Ni-O bond lengths of the six Ni-O bonds are not identical, with the bond lengths ranging from 1.979 to 2.410 Å. Four of the Ni-O bonds (two of type M1 and two of type M2 as shown in the lower-right panel of Figure 8a) are shortened to 1.979 Å while the remaining two Ni-O bonds with the O atoms in the third atomic layer are elongated to ~ 2.410 Å. However, the distortion of the Ni-substituted (100) surface is smaller than that of the Ni-substituted (110) surface. A strong distortion of the (111) surface by a Ni

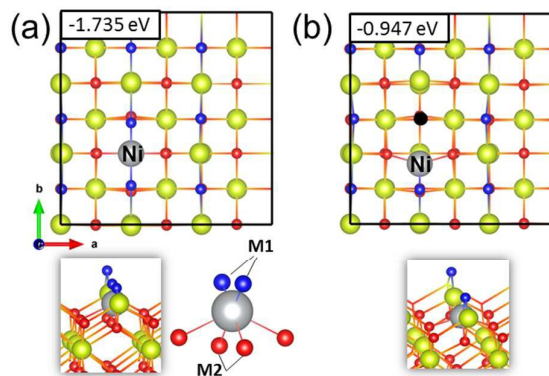


Figure 8: (a) The optimized atomic structures of the Ni-substituted CeO₂ (100) surface. The lower-left inset shows the side view of the outermost four atomic layers and the lower-right inset shows the local structure of the Ni²⁺ ion. M1 and M2 represent the magnetic O ions surrounding the Ni substituent. Ce atoms are yellow, O atoms are red and blue and Ni atom is gray. (b) The Ni-substituted CeO₂ (100) surface with a charge compensating oxygen vacancy represented by a black sphere.

substituent was also indicated by Nolan⁴⁵ in which the fluorite structure of CeO₂ does not facilitate a six- or seven- coordination environment for Ni. As a result, the large distortion around the Ni substituent leads to a nearly square planar four-coordinate

environment for the Ni substituent (see figure S16 in supporting information).

As indicated, on the Ni-substituted (110) surface, substituting a Ce^{4+} ion in CeO_2 (110) with a lower-valent cation results in a charge imbalance which is compensated by spin polarization of the oxygen ion. The Ni substituent on the (100) surface also leads to spin-polarized O atoms, resulting in unoccupied gap states ~ 0.5 eV above the top of the valence band (see figure S18 in supporting information). These states have mostly O 2p character and are spatially localized on the four nearest-neighbor O atoms of the Ni substituent (see the atoms marked by M1 and M2 in Figure 8a). The two O atoms marked by M1 and M2 in Figure 8a have a local magnetic moment of ~ 0.61 and $0.23 \mu_B$ per O atom, respectively. Here, the magnetic moment on the Ni substituent was $1.78 \mu_B$, indicating that the Ni substituent gets fully oxidized to the Ni^{2+} state. For reference, the calculated magnetic moment of Ni^{2+} in NiO was $1.65 \mu_B$. The formation energy of the Ni-substituted (100) surface was found to be -1.735 eV, while this value was found to be -0.572 eV for the (111) surface (see Table T2 in supporting information), indicating that it is easier to dope the (100) surface than the (110) and (111) surfaces, in agreement with their order of stability. The formation energy of a Ni substituent in bulk CeO_2 with a 96-atom supercell (see Figure S20 in supporting information) was calculated using equation (5).



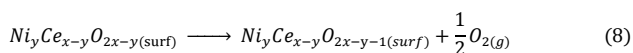
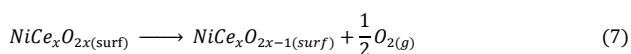
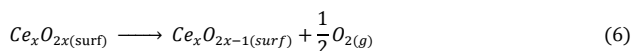
The formation energy was found to be 0.841 eV, indicating that the bulk Ni substitutional defect is thermodynamically less stable compared to Ni substitution on ceria surfaces, as shown in Figures 7 and 8. Recent experiments⁶⁵ have indicated that increasing the Ni dopant percentage in a ceria nanorod resulted in the segregation of a NiO phase and a reduction in the catalytic activity. However, we have not considered the segregation of the NiO phase in our calculations.

As concluded above, forming a ‘charge compensating’ oxygen vacancy is another means to achieve charge neutrality on a Ni-substituted surface. In order to understand better the relationship between the charge-compensating vacancy and Ni on the CeO_2 (100) surface, we have considered four possible configurations of the charge-compensating O vacancy on the Ni-substituted (100) surface (see Figure S11 in supporting information) and the most stable configuration is shown in Figure 8b. As shown in Figure 8b, the charge-compensating O vacancy prefers to be incorporated into the host matrix close to the Ni substituent. The Ni atom relaxes outward and coordinates to four O atoms. The local structure around the Ni atom was found to be asymmetric with the Ni – O bond lengths varying between 1.981 and 2.011 \AA , close to the Ni – O bond length of 2.085 \AA in $\text{NiO}_{(s)}$. We computed the O-vacancy formation energy using equation (4) to be -0.947 eV.

In fact, what is of interest in catalysis is the cost to remove the next so-called ‘active vacancy’. Hence, the formation of a second vacancy on the Ni-substituted (110) and (100) surfaces will be discussed in the next section.

C. Formation of active oxygen vacancies from pure, Ni adsorbed and Ni doped CeO_2 (110) and (100) surfaces

The effectiveness of ceria as a catalyst lies in its ability to participate in redox reactions through the creation and compensation of oxygen vacancies on the surface. Thus, any modification to the surface that results in a reduction in the energy cost associated with the creation of a surface O vacancy is expected to present a larger catalytic activity. We have computed the active O vacancy formation energy from pure, Ni-adsorbed and Ni-substituted CeO_2 (110) and (100) surfaces according to equations (6) – (8).



In equation (8), $y = 1$ for the mono-Ni substituted surface and $y = 2$ for the di-Ni substituted surface. The creation of an active O vacancy results in the partial reduction of two of the surface Ce^{4+} ions to Ce^{3+} ions. As noted earlier, a number of different distributions of Ce^{3+} ions on the surface are possible for a given vacancy location. The most stable configurations for the (110)

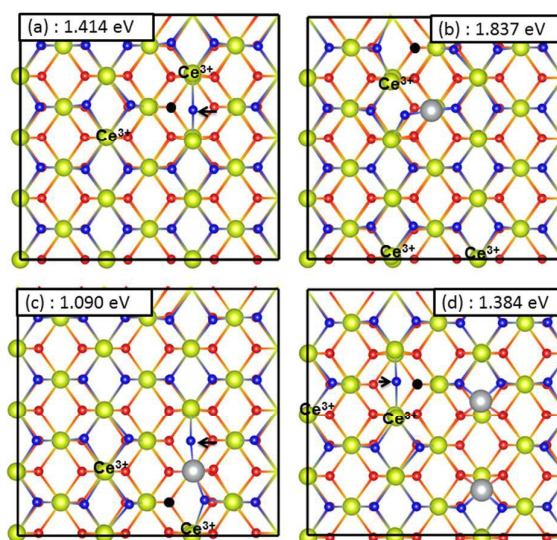


Figure 9: Active oxygen vacancy on (a) pure, (b) Ni adsorbed, (c) Mono-Ni substituted and (d) di-Ni substituted CeO_2 (110) surface. Ce^{4+} ions are yellow, Ce^{3+} ions are blue, O^{2-} ions are red and $\text{Ni}^+/\text{Ni}^{2+}$ ions are grey. The position of the oxygen vacancy is shown by black spheres. Arrows in (a), (c) and (d) show the motion of an oxygen atom from its surface site to a bridging position.

and (100) surfaces are shown in figures 9a and 10a, respectively. The formation energy of an oxygen vacancy from the pure CeO_2 (110) surface computed by us (1.414 eV) compares favourably with the value reported by Kullgren et al⁶⁴ (1.56 eV, refer to table III of their paper).

For the Ni-adsorbed (110) surface, we showed that Ni^+ and Ni^{2+} oxidation states for the adsorbate were close in energy. Thus we have investigated active O-vacancy formation beginning with both Ni^+ and Ni^{2+} configurations for the adsorbate. We have investigated two different vacancy locations for the mono-Ni substituted surface and three

different locations for the di-Ni substituted surface. For each of these locations various distributions of Ce^{3+} ions were investigated. Figure 9 shows the most favourable configuration of an active O vacancy on all the four (110) surfaces studied here while figures S5 to S8 in the supporting information show the structures and formation energies for various other vacancy positions.

For the Ni-adsorbed (100) surface, we have considered two possible configurations for the coexistence of a Ni adsorbate and active oxygen vacancy defect. As discussed above, two Ce^{3+} ions are created on the CeO_2 (100) surface by the formation of an oxygen vacancy or the adsorption of a Ni atom due to the transfer of electrons from the adsorbate or the vacancy defect to Ce^{4+} . Therefore, the coexistence of a Ni adsorbate and an oxygen vacancy is expected to lead to a partially reduced surface with four Ce^{3+} ions. The most stable configuration is shown in figure 10c while the other configurations that we have studied are shown in Figure S12 of the supporting information. The distortions around the oxygen vacancy and Ni on this surface are similar to those found around an oxygen vacancy on the pure (100) surface and Ni-adsorbed (100) surface, as shown in Figures 10a and 6a.

From Figures 9 and 10, we see that modifying the CeO_2 (110) and (100) surfaces by a Ni substitution results in a reduction in the energy cost associated with the creation of an active oxygen vacancy compared to the pristine surface, though a higher doping percentage results in a smaller change in the vacancy formation energy on the (110) surface. On the other hand, the mono-Ni adsorbate on both (110) and (100) surfaces makes it more unfavourable to create an oxygen vacancy from the surface which could lead to suppression of the activity of the catalyst. This indicates that there exists an optimal level of surface doping to achieve enhanced catalytic activity. These results are in agreement with recent experimental data which shows that increasing Ni dopant percentage beyond 7% results in a reduction in the catalytic activity of ceria nanorods⁶⁵.

For mono-Ni substituted (110) and (100) surfaces, we find that the most favourable site for oxygen vacancy formation is an oxygen ion site coordinated to the Ni dopant (see Figures 9c and 10b). On the mono-Ni substituted (110) surface, this results in significant structural rearrangement with the Ni dopant moving from a square-planar-like position to underneath a lattice metal ion site. Nolan⁴⁵ on the other hand reports the most favourable site for the creation of an active oxygen vacancy on the mono-Ni substituted (110) surface to be one of the next nearest lattice sites to the Ni dopant (see figure S7(b) in the supporting information) with a vacancy formation energy of 1.30 eV. For the same configuration, we have computed the vacancy formation energy to be 1.39 eV (see figure S7(b) in the supporting information). Furthermore, the formation of an oxygen vacancy results in the migration of a neighbouring O^{2-} ion to a bridging position on the (110) surface (figs 9a, 9c and 9d; arrows indicate the direction of motion of the oxygen atom). This rearrangement of an O^{2-} ion was not observed on the (100) surface. Comparing the formation energy of an active oxygen vacancy on the pure

(110) with (111) and (100) surfaces (1.983 and 1.679 eV respectively), we find that (110) is the most active amongst the three surfaces. However, upon doping the surface with a Ni substituent, the formation energy of an active O vacancy from the (100) surface reduced dramatically to only 0.355 eV, indicating that surface doping has a larger effect on the CeO_2 (100) surface as compared to (110).

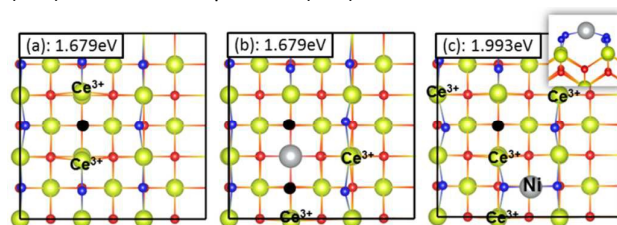


Figure 10: The optimized atomic structure of (100) surface with active oxygen vacancies. (a) Pure (100) surface, (b) Ni substituted (100) surface, (c) Ni adsorbed (100) surface. Ce atoms are yellow, Ni atoms is grey, O atoms are red and blue. The position of the O vacancy is represented by a black sphere. The inset shows the side view corresponding to the structure in panel (c).

4. Conclusions and concluding remarks

In this work, we have undertaken a systematic study of the interaction of a Ni adsorbate and Ni substituents with the CeO_2 (110) and (100) surfaces using density functional theory calculations. The following conclusions can be derived from this work:

1. A Ni atom prefers to adsorb on a bridge site as compared to a hollow site on the (110) surface, and the adsorption of Ni induces strong geometric distortions locally around the adsorbate. On the (100) surface, the most stable position of a Ni adsorbate was found to be the bridge site where the Ni atom is coordinated to two surface O atoms.
2. On a bridge site, up to 0.25 ML coverage on the (110) surface, a Ni adsorbate prefers its Ni^+ oxidation state over the Ni^{2+} oxidation state with the reduced Ce^{3+} ion located next to the Ni^+ adsorbate. Location of the Ce^{3+} ion far away from the Ni^+ adsorbate or at a subsurface position was found to be unfavourable. For the Ni^{2+} oxidation state, the most favourable distribution of Ce^{3+} ions was found to be when they were located diagonally across the Ni^{2+} adsorbate on the neighbouring sites. On the (100) surface, a Ni adsorbate prefers its Ni^{2+} oxidation state over the Ni^+ oxidation state. The Ce^{3+} ions on the (100) surface prefer to stay in the vicinity of the adsorbed Ni or the oxygen vacancy, while they prefer to separate from the Ni adatom or the oxygen vacancy on the (111) surface.
3. As the coverage of Ni on CeO_2 (110) surface increases from 0.083ML to 0.25ML, the adsorption energy for the most favourable configuration, i.e., Ni^+ on a bridge site, decreases from -0.449 eV to -0.322 eV.
4. With increase in coverage of Ni from 0.083ML to 0.25ML, the stabilization of the Ni^+ oxidation state over the Ni^{2+} oxidation state on a bridge site decreases from ca. 49 meV to

21 meV for the most preferred Ce³⁺ ion distribution in the respective oxidation states of the Ni adsorbate.

5. Adsorption of Ni introduces split-off-states above the CeO₂ (110) and (100) valence band. In its Ni⁺ oxidation state on the (110) surface, these states arise from the *f* orbital on the reduced Ce³⁺ ion, the *d* orbital of the Ni⁺ adsorbate and the *p* orbital of the oxygen ions that are coordinated to the Ni⁺ adsorbate. However, in its Ni²⁺ oxidation state on both (110) and (100) surfaces, these states arise from the *f* orbitals on the two reduced Ce³⁺ ions only.

6. In contrast to Ni adsorption, a Ni substituent does not induce the reduction of a Ce⁴⁺ to Ce³⁺. However, it induces strong structural distortion locally, with the Ni substituent moving into a four-coordinated nearly planar environment from the six-coordinated metal ion site on the (110) surface.

7. The nearest neighbour locations were found to be the most favourable distribution of the two Ni substituents on the (110) surface. Further, this resulted in spontaneous ejection of an O₂ molecule from the surface.

8. Substitution of surface Ce atoms by Ni atoms resulted in a reduction in the energy required to create an active oxygen vacancy while a Ni adsorbate caused an increase in the formation energy of an active O vacancy. The degree of reduction in the vacancy formation energy points to the presence of an optimum level of surface doping to achieve enhanced catalytic activity.

The effect of these surface modifications on the catalytic activity of Ceria catalysts for WGS and methanation reactions is a subject of an ongoing study in our group.

Notes

W.Q. Li and S.G.S are joint first authors in this article.

Acknowledgements

The authors acknowledge the computational resources provided by WestGrid and Compute Canada for this work. Discovery Grant funding (project RGPIN-2014-06606) from NSERC (Canada) to D.R.S and funding from European Research Council (ERC StGC3ENV) are gratefully acknowledged. W.L. acknowledges support from the Marie Cuire IRSES project TEMM1P.

References

- 1 A. Trovarelli, *Catalysis Reviews*, 1996, **38**, 439-520.
- 2 A. Trovarelli, C. de Leitenburg, M. Boaro and G. Dolcetti, *Catal. Today*, 1999, **50**, 353-367.
- 3 R. J. Gorte, *AIChE J.*, 2010, **56**, 1126-1135.
- 4 Q. Fu, A. Weber and M. Flytzani-Stephanopoulos, *Catal. Lett.*, 2001, **77**, 87-95.
- 5 Q. Fu, H. Saltsburg and M. Flytzani-Stephanopoulos, *Science*, 2003, **301**, 935-938.

- 6 S. P. S. Badwal, D. Fini, F. T. Ciacchi, C. Munnings, J. A. Kimpton and J. Drennan, *Journal of Materials Chemistry A*, 2013, **1**, 10768-10782.
- 7 M. V. Ganduglia-Pirovano, C. Popa, J. Sauer, H. Abbott, A. Uhl, M. Baron, D. Stacchiola, O. Bondarchuk, S. Shaikhutdinov and H.-J. Freund, *J. Am. Chem. Soc.*, 2010, **132**, 2345-2349.
- 8 T. Kropp, J. Paier and J. Sauer, *J. Am. Chem. Soc.*, 2014, **136**, 14616-14625.
- 9 S. Carrettin, P. Concepción, A. Corma, J. M. López Nieto and V. F. Puntes, *Angew. Chem. Int. Ed.*, 2004, **43**, 2538-2540.
- 10 T. Bunluesin, E. S. Putna and R. J. Gorte, *Catal. Lett.*, 1996, **41**, 1-5.
- 11 T.-S. Nguyen, F. Morfin, M. Aouine, F. Bosselet, J.-L. Rousset and L. Piccolo, *Catal. Today*, 2015, **253**, 106-114.
- 12 T. Bunluesin, R. J. Gorte and G. W. Graham, *Applied Catalysis B: Environmental*, 1998, **15**, 107-114.
- 13 Y. Li, Q. Fu and M. Flytzani-Stephanopoulos, *Applied Catalysis B: Environmental*, 2000, **27**, 179-191.
- 14 S. Hilaire, X. Wang, T. Luo, R. J. Gorte and J. Wagner, *Applied Catalysis A: General*, 2001, **215**, 271-278.
- 15 J. A. Rodriguez, P. Liu, J. Hrbek, J. Evans and M. Pérez, *Angew. Chem. Int. Ed.*, 2007, **46**, 1329-1332.
- 16 G. Zhou, L. Barrio, S. Agnoli, S. D. Senanayake, J. Evans, A. Kubacka, M. Estrella, J. C. Hanson, A. Martínez-Arias, M. Fernández-García and J. A. Rodriguez, *Angew. Chem. Int. Ed.*, 2010, **49**, 9680-9684.
- 17 L. Barrio, A. Kubacka, G. Zhou, M. Estrella, A. Martínez-Arias, J. C. Hanson, M. Fernández-García and J. A. Rodriguez, *J. Phys. Chem. C*, 2010, **114**, 12689-12697.
- 18 S. Senanayake, J. Evans, S. Agnoli, L. Barrio, T.-L. Chen, J. Hrbek and J. Rodriguez, *Top. Catal.*, 2011, **54**, 34-41.
- 19 J. Carrasco, L. Barrio, P. Liu, J. A. Rodriguez and M. V. Ganduglia-Pirovano, *J. Phys. Chem. C*, 2013, **117**, 8241-8250.
- 20 J. Carrasco, D. López-Durán, Z. Liu, T. Duchoň, J. Evans, S. D. Senanayake, E. J. Crumlin, V. Matolín, J. A. Rodríguez and M. V. Ganduglia-Pirovano, *Angew. Chem. Int. Ed.*, 2015, **54**, 3917-3921.
- 21 J. Paier, C. Penschke and J. Sauer, *Chem. Rev.*, 2013, **113**, 3949-3985.
- 22 S. J. Tauster, *Acc. Chem. Res.*, 1987, **20**, 389-394.
- 23 J. A. Farmer and C. T. Campbell, *Science*, 2010, **329**, 933-936.
- 24 G. L. Haller and D. E. Resasco, *Adv. Catal*, 1989, **36**, 173-235.
- 25 M. Nolan, S. Grigoleit, D. C. Sayle, S. C. Parker and G. W. Watson, *Surf. Sci.*, 2005, **576**, 217-229.
- 26 M. M. Branda, N. C. Hernández, J. F. Sanz and F. Illas, *J. Phys. Chem. C*, 2010, **114**, 1934-1941.
- 27 L. Szabová, M. F. Camellone, M. Huang, V. Matolín and S. Fabris, *J. Chem. Phys.*, 2010, **133**, 234705.
- 28 Z. S. Lu, Z. X. Yang and K. Hermansson, 2011.
- 29 Y. Tang, H. Zhang, L. Cui, C. Ouyang, S. Shi, W. Tang, H. Li and L. Chen, *J. Power Sources*, 2012, **197**, 28-37.

- 30 Z. P. Liu, S. J. Jenkins and D. A. King, *Phys. Rev. Lett.*, 2005, **94**, 196102.
- 31 Z. Yang, Z. Lu and G. Luo, *Phys. Rev. B*, 2007, **76**, 075421.
- 32 A. Bruix, K. M. Neyman and F. Illas, *J. Phys. Chem. C*, 2010, **114**, 14202-14207.
- 33 Z. S. Lu and Z. X. Yang, *J. Phys.: Condens. Matter*, 2010, **22**, 475003.
- 34 A. D. Mayernick and M. J. Janik, *J. Chem. Phys.*, 2009, **131**, 084701.
- 35 M. M. Branda, N. J. Castellani, R. Grau-Crespo, N. H. de Leeuw, N. C. Hernandez, J. F. Sanz, K. M. Neyman and F. Illas, *J. Chem. Phys.*, 2009, **131**, 094702.
- 36 H.-X. Mai, L.-D. Sun, Y.-W. Zhang, R. Si, W. Feng, H.-P. Zhang, H.-C. Liu and C.-H. Yan, *J. Phys. Chem. B*, 2005, **109**, 24380-24385.
- 37 R. Si and M. Flytzani-Stephanopoulos, *Angew. Chem. Int. Ed.*, 2008, **47**, 2884-2887.
- 38 L. Cui, Y. Tang, H. Zhang, L. G. Hector, C. Ouyang, S. Shi, H. Li and L. Chen, *PCCP*, 2012, **14**, 1923-1933.
- 39 M. Nolan, *J. Chem. Phys.*, 2012, **136**, 134703.
- 40 X. Du, D. Zhang, L. Shi, R. Gao and J. Zhang, *J. Phys. Chem. C*, 2012, **116**, 10009-10016.
- 41 W. Tang, Z. Hu, M. Wang, G. D. Stucky, H. Metiu and E. W. McFarland, *J. Catal.*, 2010, **273**, 125-137.
- 42 D. García Pintos, A. Juan and B. Irigoyen, *J. Phys. Chem. C*, 2013, **117**, 18063-18073.
- 43 M. Nolan, *J. Phys. Chem. C*, 2009, **113**, 2425-2432.
- 44 Y. Irene and N. Michael, *J. Phys.: Condens. Matter*, 2010, **22**, 135004.
- 45 M. Nolan, *J. Mater. Chem.*, 2011, **21**, 9160-9168.
- 46 G. Kresse and J. Hafner, *Phys. Rev. B*, 1993, **47**, 558-561.
- 47 G. Kresse and J. Hafner, *Phys. Rev. B*, 1994, **49**, 14251-14269.
- 48 G. Kresse and J. Furthmüller, *Comput. Mater. Sci.*, 1996, **6**, 15-50.
- 49 G. Kresse and J. Furthmüller, *Phys. Rev. B*, 1996, **54**, 11169-11186.
- 50 P. E. Blöchl, *Phys. Rev. B*, 1994, **50**, 17953-17979.
- 51 G. Kresse and D. Joubert, *Phys. Rev. B*, 1999, **59**, 1758-1775.
- 52 S. L. Dudarev, G. A. Botton, S. Y. Savrasov, C. J. Humphreys and A. P. Sutton, *Phys. Rev. B*, 1998, **57**, 1505-1509.
- 53 M. Cococcioni and S. de Gironcoli, *Phys. Rev. B*, 2005, **71**, 035105.
- 54 X. Wang, M. Shen, J. Wang and S. Fabris, *J. Phys. Chem. C*, 2010, **114**, 10221-10228.
- 55 J. Graciani, A. M. Márquez, J. J. Plata, Y. Ortega, N. C. Hernández, A. Meyer, C. M. Zicovich-Wilson and J. F. Sanz, *J. Chem. Theory Comput.*, 2011, **7**, 56-65.
- 56 W.-B. Zhang, N. Yu, W.-Y. Yu and B.-Y. Tang, *Eur. Phys. J. B*, 2008, **64**, 153-158.
- 57 J. P. Allen and G. W. Watson, *PCCP*, 2014, **16**, 21016-21031.
- 58 N. V. Skorodumova, M. Baudin and K. Hermansson, *Phys. Rev. B*, 2004, **69**, 075401.
- 59 P. Pulay, *Chem. Phys. Lett.*, 1980, **73**, 393-398.
- 60 N. V. Skorodumova, M. Baudin and K. Hermansson, *Phys. Rev. B*, 2004, **69**, 075401.
- 61 M. Molinari, S. C. Parker, D. C. Sayle and M. S. Islam, *J. Phys. Chem. C*, 2012, **116**, 7073-7082.
- 62 T. Kropp and J. Paier, *J. Phys. Chem. C*, 2015, **119**, 23021-23031.
- 63 W. Song and E. J. M. Hensen, *J. Phys. Chem. C*, 2013, **117**, 7721-7726.
- 64 J. Kullgren, K. Hermansson and C. Castleton, *J. Chem. Phys.*, 2012, **137**, 044705.
- 65 A. Romero-Nunez and G. Diaz, *RSC Advances*, 2015, **5**, 54571-54579.